RSC Advances

ROYAL SOCIETY OF CHEMISTRY

www.rsc.org/advances

Journal Name

ARTICLE

Stabilising Mn₃O₄ Nanosheet on Graphene *via* Forming 2D-2D Nanostructure for Improvement of Lithium Storage

Yanhong Zhao,[a,b] Gang Chen,[a]* Chunshuang Yan,[a] Chade Lv,[a] Rui Wang[a] and Jingxue Sun[a]

A 2D-2D nanostructured Mn_3O_4 nanosheet (Mn_3O_4-NS)/ graphene sheet (GNS) composites are synthesized by a simple liquid-phase route, in which mica-like Mn_3O_4 and GNS are assembled into a robust structure *via* face contacting. The sheet-on-sheet coupled with high stability between Mn_3O_4-NS and GNS significantly promotes the interfacial electron and lithium ion transport, as well as accommodates volume change. It is believed that the mechanical stability and electrical conductivity of Mn_3O_4-NS are increased by GNS, the aggregation or restacking of which to GNS, on the other hand, effectively prevented by Mn_3O_4-NS. When used as a negative electrode for lithium ion batteries, the hybrid composites deliver a higher specific capacity, enhanced rate capability and excellent cyclic stability than that of independent Mn_3O_4-NS and GNS.

1 Introduction

Lithium ion batteries (LIBs) have attracted considerable interest as a power source for consumer electronics and electric vehicles owing to their unique properties such as attractive high energy density, cycling stability, and excellent rate capability.[1-3] Although graphite anodes are now widely used in commercial LIB due to high cyclability, their low capacity (372 mA h g⁻¹) has not been able to meet the increasing demand for next generation batteries with higher capacity yet.[4] Transitional metal oxides, such as Mn_3O_4 have been suggested as promising alternative anode materials arising from their theoretical capacities (937 mA h g⁻¹) higher than those of graphite (372 mA h g⁻¹).[5-6] The material, however, is still hampered due to the poor electrical conductivity and large volume variation during lithium uptake/release, resulting in a large irreversible capacity fade and poor cycling performance.[7-9]

To date, enormous effort has been made to tackle these drawbacks. One effective strategy is to synthesize nanostructured Mn_3O_4 (nanofibers,[10] nanorods[11]) to shorten the diffusion length of electrons and lithium ions. Besides, uses of their composites with carbonaceous materials are also the efficient methods to improve the cycling stability of Mn_3O_4 by suppressing their volume change and increasing their electrical conductivity.[12] Graphene is proposed as one of the most appealing carbon materials with intrinsically excellent electrical conductivity and mechanical flexibility.[13-15]

A variety of Mn_3O_4 nanomaterials with different synthesis systems have been blended with graphene as anode materials and have improved the capacity, rate capability, and cycling stability.[16-17] For example, Li *et al.*[18] synthesize a composite of Mn_3O_4 nanoparticle (0D) wrapped in graphene sheets using a microwave-assisted hydrothermal method, presenting high reversible capacity (more than 900 mA h g⁻¹ at 40 mA g⁻¹). Lee *et al.*[19] prepare Mn_3O_4 nanorods (1D) on graphene sheets by a hydrothermal reaction from $KMnO_4$. Chen *et al.*[20] and Luo *et al.*[21] report the Mn_3O_4 nanosheets (2D) on the graphene without discussing their composite structure and effections for electrochemical performances.

However, in comparison with above composites (0D-2D and 1D-2D composites), a 2D-2D composite is a more ideal choice due to its large contact surface, resulting in exhibiting higher stability. On the other hand, a heavy agglomeration of graphene may take place upon repetitive cycling with lithium ions and even in the drying process of graphene electrodes. Thus, 2D-2D hybrid can reduce the contact between graphene nanosheets more effectively compared to 0D or 1D "separator" materials. Sun *et al.*[22] discuss the 2D structure of sheet-on-sheet composite, which precedes the 1D structure of nannoparticles on graphene. Based on the above, we consider that a sheet-on-sheet (Mn_3O_4-NS/GNS) nanostructure is beneficial for ions and electrons to access their surface, consequently enabling a fast conversion reaction and structure stability.

Herein, a 2D-2D structured Mn_3O_4-NS/GNS composite is prepared by using a simple facile solution phase reaction method under room temperature. Meanwhile, the formation mechanism of the 2D-2D structures is proposed and discussed. The graphene sheets in the composite can not only efficiently buffer the volume change of Mn_3O_4 nanosheets, but also preserve the high electrical conductivity. In addition, the

[a] *Department of Chemistry, Harbin Institute of Technology, Harbin 150001, China. Email: gchen@hit.edu.cn.*
[b] *College of Enviromental and Chemical Engineering, Heilongjiang University of Science and Technology, Harbin 150022, China, Email: zhaoyh08@126.com*
[c] *Electronic Supplementary Information (ESI) available: See DOI*

configuration, Mn_3O_4 nanosheet coupling graphene, will also greatly enhance the electrochemical performance due to increased structure stability and charge transfer rate. As a consequence, the composites exhibit the outstanding discharge/charge capacity, good cycle life, and high rate capability as anode material for LIBs. To the best of our knowledge, it is one of the best performances for Mn_3O_4 as an anode.

2 Experimental section

2.1 Materials

Nature graphite, Sodium nitric acid ($NaNO_3$), sulfuric acid (98% H_2SO_4), potassium permanganate ($KMnO_4$), hydrogen peroxide (30% H_2O_2), manganese acetate ($Mn(OAc)_2 \cdot 4H_2O$), sodium hydroxide (NaOH), and hydrazine hydrate (80% $N_2H_4 \cdot H_2O$) were purchased from TianJin Chemical Reagent Co.. All the chemicals of analytical grade were not be processed again.

2.2 Synthesis of Mn_3O_4 and Mn_3O_4-NS/GNS

Mn_3O_4 nanosheet (Mn_3O_4-NS) was synthesized by a simple liquid precipitation method. The 2 mmol manganese acetate was first dissolved in 50 ml distilled water. During the solution was stirred by a magnetic apparatus, the 100 ml sodium hydroxide solution (0.1 mol L^{-1}) was slowly dropped at a rate of a drop every 5 second, and the reaction was controlled to end after 120 min. The brown precipitate was washed with distilled water at least 5 times, filtered and dried at 80 ^{o}C overnight. Finally , the product of brown powder was achieved after heating at 300 ^{o}C for 2 h in nitrogen.

The composite of Mn_3O_4-NS/GNS was prepared with the same method. Instead of distilled water, the 2 mmol manganese acetate was dissolved in 50 ml of 10 mg ml^{-1} graphene oxide solution (obtained by Hummer's method). After the brown precipitate was washed, the composite was reduced by 5 ml $N_2H_4 \cdot H_2O$ at 98 ^{o}C for 1 h in a water bath. Then, the black powder was obtained after heat treatment.

2.3 Materials characterization

The structure of prepared materials were characterized by powder X-ray diffractometer (Bruker D8 Advance with Cu Kα, λ=0.15406 nm, 40 kV, 40 mA) in the 2 theta range of 10-70º, Microscopes Raman Spectrometer (British Renishaw, ladar: 532 nm), and X-ray photoelectron spectroscopy (XPS) measurements were performed on a PHI 5700 XPS/ESCA system with a monochromatic Al Kα (1486.6 eV). The morphology of the products were obtained using field emission scanning electron microscopy (FESEM, FEI Quanta 200F), transmission electron microscopy (TEM, FEI Tecnai G2 S-Twin, 300 kV) and atomic force microscope (AFM, Dimension Icon). The thermal analysis was conducted in a thermogravimetric analysis system (STA7300, HITACHI) under flow of air (200 cm^3 min^{-1}), at a heating rate of 10 ^{o}C min^{-1} from 30 ^{o}C to 600 ^{o}C. Nitrogen adsorption–desorption measurements were performed on an V-Sorb 2800 surface analyzer at 77.35 K.

2.4 Electrochemical measurements

The working electrodes were prepared by a slurry (80 wt% active material, 10 wt% polyvinylidene fluoride (PVDF) in N-methyl pyrrolidone (NMP), and 10 wt% carbon black) coating procedure. Test cells (2025 type) were assembled in an argon-filled glove box with the metallic lithium foil as the reference and counter electrodes. The electrolyte was 1.0 mol dm^{-3} $LiPF_6$ in a mixture of ethylene carbonate (EC) and dimethyl carbonate (DMC). The galvanostatically charged and discharged processes were measured in the range of 0.01-3.0 V (vs. Li/Li$^+$) at room temperature using a NEWARE battery test system. Cyclic voltammogram (CV) measurements were measured on a CHI660C electrochemical workstation at a scan rate of 0.5 mV s^{-1}. And AC impedance measurement was carried out using the same electrochemical working station in the 100 KHz to 10 mHz frequency range.

3 Results and discussion

Mn_3O_4 and Mn_3O_4-NS/GNS composites are characterized by XRD patterns as shown in Fig. 1. The peaks of Mn_3O_4 are accorded with the tetragonal structure Mn_3O_4 (JCPDS card No.80-0382, space group I41/*amd*), suggesting a purity of Mn_3O_4 samples. The diffraction peak of Mn_3O_4-NS/GNS are almost corresponding with Mn_3O_4 except the broader peak at about 25°, indicating the diffraction of reduction graphene. No impurities are detected in the XRD patterns, and the sharp peaks indicate that the synthesized products are well-crystallized.

And the presence of reduction graphene and Mn_3O_4 can be confirmed from typical peaks in the Raman spectra (Fig. 2a). A prominent peak observed at 645 cm^{-1} is according with the spectra for crystalline Mn_3O_4. The G band (1594 cm^{-1}) corresponds to the ordered sp^2 bonded carbon, whereas the D band (1342 cm^{-1}) is ascribed to edges amount or disordered layers. The D/G intensity ratio (I_D/I_G = 0.88) of Mn_3O_4-NS/GNS composite is larger than GO (graphene oxide, I_D/I_G = 0.85), indicating the increasing of disordered degree of carbon and the partial reduction of carbon in the sample.[23] Furthermore, the existence of oxygenic functional group in the composite can increase the interlayer spacing of graphene sheets, preventing the reuniting of graphene. The prepared 2D-2D
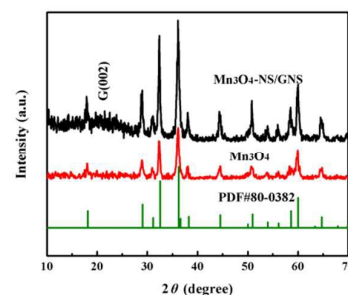
Fig. 1 X-Ray diffraction patterns of Mn_3O_4 and Mn_3O_4-NS/GNS composite.
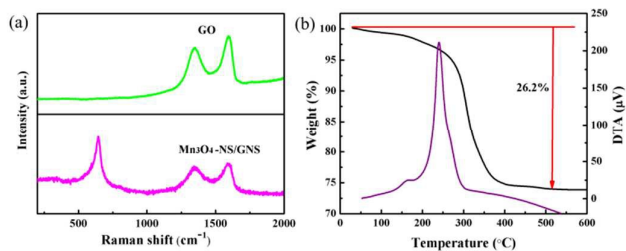
Fig. 2 Raman spectra of GO and Mn₃O₄-NS/GNS composite (a) and TG-DTA curves of 2D-2D Mn₃O₄-NS/GNS composite in air (b).

structure will keep the structural stability of Mn₃O₄-NS/GNS. To confirm the content of reduction graphene oxide, the thermogravimetric analysis (TGA) is carried out in air. Fig. 2b shows that the weight loss of Mn₃O₄-NS/GNS composite is 26.2% and the exothermic reaction is caused by carbon oxidized. From the result, we can approximately calculate the mass content of Mn₃O₄ in the composite is 73.8%.

The prepared samples of Mn₃O₄ are further investigated by TEM and the results are presented in Fig. 3. The low magnified TEM images in Fig. 3a and b present the full view of the morphology. The Mn₃O₄ nanocrystals show a mica-like morphology. It can be found that the edge of nanosheets is irregular, the thickness of the nanosheets is about 10-20 nm and the diameter of the Mn₃O₄ nanosheets is around 60-100 nm. The X-ray energy dispersive spectroscopy (EDS) spectrum shows only two elements of Mn and O in the prepared samples (Fig. 3d). As showed in images, the 2D sheet nanostructure will provide large surface area to contact with electrolyte, which benefits to improve the electrochemical performances.[24] The corresponding HRTEM in Fig. 3c confirms the high crystallinity. The lattice fringes with a spacing of 0.276 nm and 0.248 nm are assigned to the planes of (103) and (211).
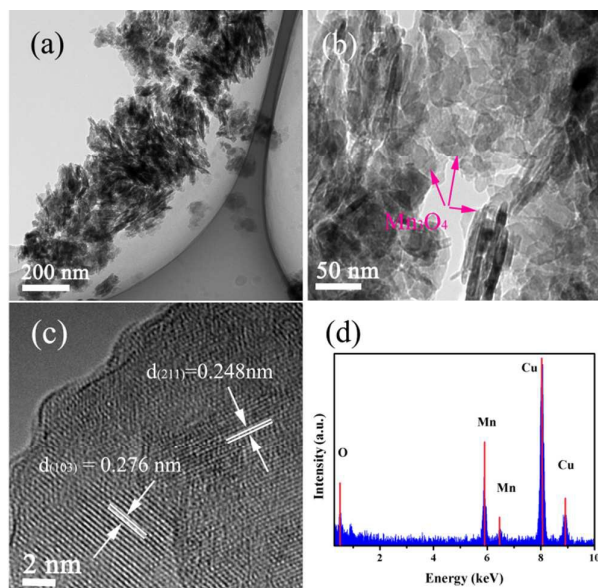
Fig. 3 TEM micrographs of mica-like Mn₃O₄ nanosheets. (a) low magnification, (b) high magnification, (c) an HRTEM image, (d) EDS spectrum of mica-like Mn₃O₄.
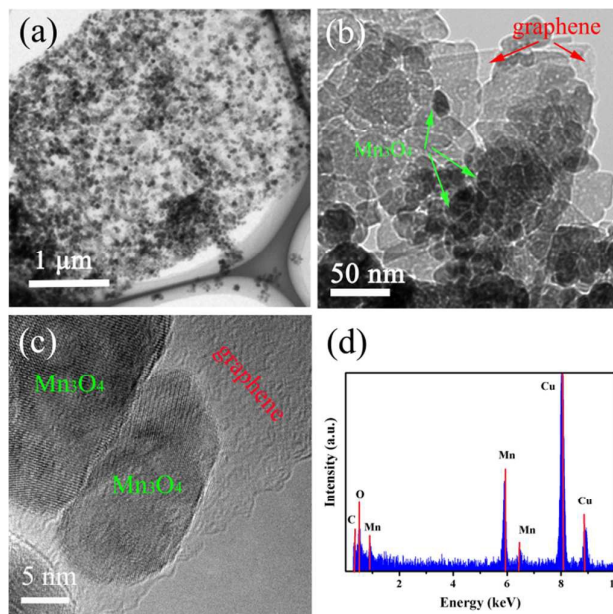
Fig. 4 TEM images of Mn₃O₄-NS/GNS composite. (a) low magnification,(b) high magnification, (c) an HRTEM image of Mn₃O₄-NS/GNS 2D-2D structure, (d) EDS spectrum of Mn₃O₄-NS/GNS.

As a comparison, the TEM images of Mn₃O₄-NS/GNS are showed in Fig. 4. Fig. 4a and b indicate that the Mn₃O₄ nanosheets are uniformly embed in the silk-like graphene sheets. The scale of Mn₃O₄ nanosheets in the composite are consistent with the pure Mn₃O₄, which can be explained with the same synthesis method and the addition of graphene is only as the supporting structure. The EDS spectrum in Fig. 4d suggests the synthesized products are composed of Mn, O, and C elements. As showed in Fig. 4c, the combination of 2D nanosheet Mn₃O₄ with 2D graphene sheet is the face to face contact, which precede the point contact and line contact in electrochemical reaction.[25] While, the thickness of the Mn₃O₄ nanosheets can be observed by AFM image in Fig. 5. That is around 20 nm, the thickness is larger than the result of TEM. This can be attributed to multi-sheets stacking combined with the TEM images of Fig. 3 and Fig. 4. Therefore, we infer that the sheet-on-sheet tight combination of Mn₃O₄ nanosheet and graphene is beneficial to transfer electron and buffer volume variation of Mn₃O₄ in charge and discharge process, resulting in the excellent electrochemical performance.

In addition, the chemical composition of the Mn₃O₄-NS/GNS composite are confirmed by XPS (Fig. 6). In the survey range (0-1000 eV), carbon, manganese, and oxygen are detected.
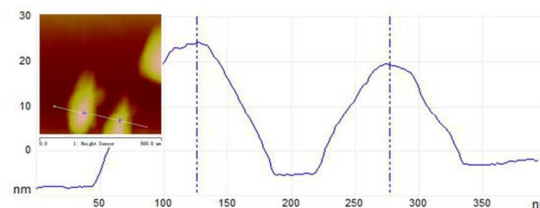
Fig. 5 AFM images of the Mn₃O₄-NS/GNS composite.
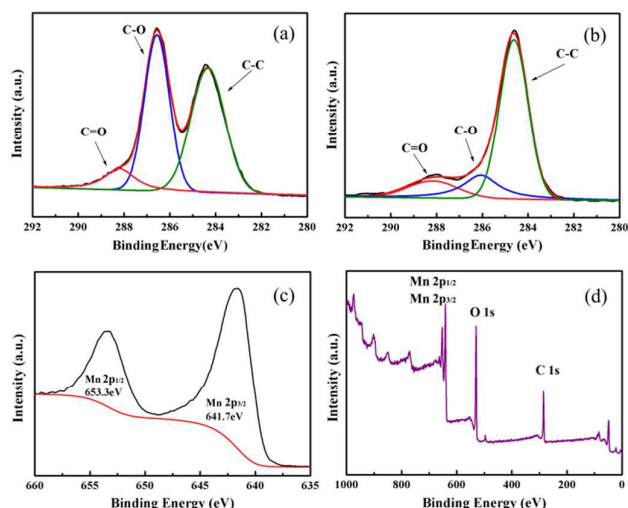
Fig. 6. XPS spectra for the C 1s regions of (a) graphene oxide before compositing, (b) Mn_3O_4-NS/GNS after compositing, (c) Mn 2p region of Mn_3O_4-NS/GNS and (d) survey of composite.

The peaks in the spectra of Fig. 6a and 6b are composed of three chemical states of carbon. It can be attributed to carbon sp^2 bonding (C-C), epoxide/hydroxyl groups (C=O), and carbonyl/carboxyl groups (C-O),[21] at 288.2, 286.3 and 284.6 eV respectively.[26] Obviously, the strongest peak in Fig. 6a is carbonyl (C-O), indicating the presence of oxygen containing functional groups. They would become the active site where the Mn_3O_4-NS/GNS composite will be produced through electrostatic attraction in the reaction solution. On the contrary, the strongest peak in Fig. 6b becomes carbon sp^2 bonding (C-C), which is because of the reduction of GO and the self-assembled formation of Mn_3O_4 nanosheets on graphene sheets. The Mn 2p spectrum of Mn_3O_4-NS/GNS composite is presented in Fig. 6c, where the peaks of Mn $2p_{3/2}$ (641.7 eV) and Mn $2p_{1/2}$ (653.3 eV) are observed. They have a spin energy separation of 11.6 eV in good accordance with the reported datum on Mn_3O_4,[27] which confirms the existence of Mn_3O_4 in the composite.
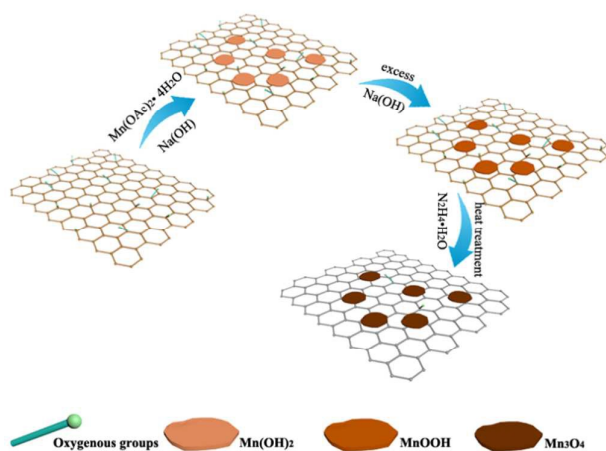
Fig. 7 Schematic illustration of the proposed growth procedure of 2D-2D Mn_3O_4-NS/GNS composites.

Based on the analysis above, the formation machnism of 2D-2D Mn_3O_4-NS/GNS nanostructure is shown in Fig. 7. The $Mn(OH)_2$ nanosheet is achieved in the presence of graphene oxide (GO) by a simple facile solution phase reaction method. The possible linkage between surface groups (hydroxyl and carboxyl) of $Mn(OH)_2$ and GO may promote the formation of a sheet-on-sheet composite. Subsequently, $Mn(OH)_2$ nanosheet is oxidized to MnOOH nanosheet through excess hydroxyl and oxygen in the air. After hydrazine hydrate reducing, unique Mn_3O_4-NS/GNS sheet-on-sheet nanostructures are obtained *via* topotactic conversion. The chemical reactions of forming the composite can be expressed as follows:

$$Mn^{2+} + 2OH^- \rightarrow Mn(OH)_2 \qquad (1)$$
$$4Mn(OH)_2 + O_2 \rightarrow 4MnOOH + 2H_2O \qquad (2)$$
$$12MnOOH + N_2H_4 \rightarrow 4Mn_3O_4 + 8H_2O + N_2 \qquad (3)$$
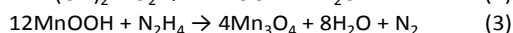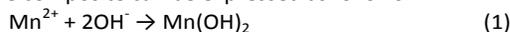
For testifying the superiority of Mn_3O_4-NS/GNS composite, their electrochemical performances are evaluated by installing coin type cell. Fig. 8a and 8b show that the galvanostatic charge and discharge profiles of the as-prepared samples at a current density of 50 mA g^{-1} in the potential range from 0.01 to 3 V *vs* Li/Li^{+}. As compared, the electrochemical performances of GN are showed in Fig.S2. It can be found that Mn_3O_4-NS/GNS composite delivers a high reversible specific capacity compared with the Mn_3O_4.[10] The discharge and charge capacities of the mica-like Mn_3O_4 are 954.02 and 530.99 mA h g^{-1}. While, the discharge and charge capacities of the Mn_3O_4-NS/GNS composite are 1890.56 and 1002.95 mA h g^{-1}. The reversible capacity of the composite exceeds 100 mA h g^{-1} than the capacity of the others' made by Li and Ma *et al*.[18,28] The capacity loss in the first cycle is mainly due to the formation of a solid electrolyte interface (SEI) layer.[29,30] The cyclic voltammetry of Mn_3O_4-NS/GNS composite is showed in Fig. 8c, which is tested in the potential range from 3.0 to 0.01 V vs Li/Li^{+} at room temperature. In the first scan, a broad reduction peak at about 1 V is observed and disappears afterwards, which is ascribed to the decomposition of electrolyte and formation of SEI films.[31] An intense peaks at low potential is
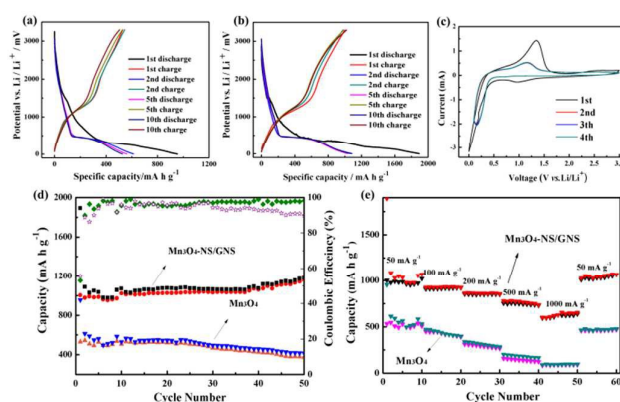
Fig. 8. Electrochemical characterization of mica-like Mn_3O_4 and Mn_3O_4-NS/GNS composite as electrode materials, (a) Galvanostatic charge and discharge curves for Mn_3O_4; (b) Mn_3O_4-NS/GNS composite at a current density of 50 mA g^{-1} for various cycles (1st, 2nd, 5th and 10th); (c) Cyclic voltammograms of the 1st, 2nd, 3rd and 4th cycles of Mn_3O_4-NS/GNS composite (scan rate 0.5 mV s^{-1}); (d) capacity retentions of two samples for 50 cycles at 50 mA g^{-1}; (e) rate capability of Mn_3O_4-NS/GNS composite at various current densities.

attributed to the subsection reduction of manganese oxide to metallic manganese,[32] which is concurrent with the change of first discharge curve after 0.5 V in Fig. 8b. The oxidation peaks are occurred at 1.34 V and 2.2 V, which are assigned to Mn^0 to Mn^{2+} and further oxided from Mn^{2+} to Mn^{3+}, respectively.[33] The good reversibility and stability of the Mn_3O_4-NS/GNS composite can be demonstrated by the almost identical oxidation and reduction behaviors from the 2nd cycle to 4th cycle.

The different cycling performances of two samples at 50 mA g^{-1} are shown in Fig. 8d. Mn_3O_4-NS/GNS composite processes the excellent reversible capacity, which reach 1180.54 mA h g^{-1} after 50th cycles (Fig. 8d). The high capacity of the composite even exceeds the theory capacity (835 mA h g^{-1}), which is calculated by results of the TGA measurements as shown below:[34]

Mn_3O_4-NS/GNS:

26.2 wt%×744 mA h g^{-1} +73.8 wt%×937 mA h g^{-1}

= 835 mA h g^{-1} (4)

The cycling performance of the composite is optimized after being designed for the 2D-2D structure. For Mn_3O_4, the capacity is gradually decreasing because of the loss of electric contact with the volume changing.[35] The rate capability of Mn_3O_4-NS/GNS materials is evaluated at current rates of 100, 200, 500 mA g^{-1} and 1000 mA g^{-1} (Fig. 8e). Even at 1000 mA g^{-1}, the charge capacity of composite can maintain 637.44 mA h g^{-1} which is far eminent compared with the resported.[36-38] The stable 2D-2D structure of Mn_3O_4-NS/GNS composite is attribute to face to face contact through Mn_3O_4 nanosheets and graphene sheets, preceding point contact and line contact. Apparently, the improved capacity and excellent rate capability are benefited from the stability of sheet-on-sheet (2D-2D) structure, which provides a large contact area for electron transmission and Li ion diffusion.

To test the improved electrochemical performances of Mn_3O_4-NS/GNS composite with 2D-2D structure, the electrochemical impedance spectroscopy (EIS) is measured in Fig. S3. It shows the patterns for mica-like Mn_3O_4 and Mn_3O_4-NS/GNS composite at same voltage at 0.5 mV s^{-1}. To comprehend the resistance effect of cell made by composite, simple simulative circuit is constructed to explain the component of resistance. The inset of Fig. S3a is the equivalent circuit of mica-like Mn_3O_4 and Mn_3O_4-NS/GNS composite as

Fig. 9 Typical nitrogen adsorption–desorption isotherm and the inset corresponding pore-size distribution, (a) Mn_3O_4 and (b) Mn_3O_4-NS/GNS composite.

the electrode material, the total resistance is composed of electrolyte resistance (Re), surface film resistance (Rs), charge transfer resistance (Rc) and Warburg impedance (Rw), the Qs and Qc are the corresponding capacitances of Rs and Rc. According the simulative circuit, the charge transfer resistance can be calculated. They are 43.62 Ω and 34.16 Ω, corresponding to the resistance of Mn_3O_4 and the as-prepared composite. The smaller charge transfer resistance of the Mn_3O_4-NS/GNS composite is beneficial to improve electrochemical performances.

The Nyquist plot comprise of a semicircle corresponding high frequency region and a sloping line corresponding low frequency region. The sloping line is attributed to the diffusion of lithium ion into the state of the electrode material, which is called as Warburg diffusion. The diffusion coefficient of lithium ion can be calculated from the plots in the low-frequency region according to the following equation:[39]

$$D = (R^2T)^2/(2A^2n^4F^4C^2\sigma^2) \qquad (5)$$

where R is the gas constant, T is the absolute temperature, n is the number of electron (s) per molecule oxidized, A is the surface area, F is Faraday's constant, C is the concentration, D is the diffusion coefficient, and σ is the Warburg factor which has relationship with Z_{re} as follows:[40,41]

$$Z_{re}= R_D +R_L + \sigma\omega^{-1/2} \qquad (6)$$

$$\omega = 2\pi f \qquad (7)$$

The relationship between Z_{re} and the reciprocal square root of frequency in the low-frequency (f) region is shown in Fig. S3b (Mn_3O_4) and 3c (Mn_3O_4-NS/GNS composite). The number of the slope can be read from the fitted curve and Warburg coefficient is the slope of the line. The calculation results of σ are 82.96 and 14.34, corresponding to Mn_3O_4 and Mn_3O_4-NS/GNS. In the equation (5), the Li^+ diffusion coefficient (D) is proportional to σ^2. So, we can obtain the values of D for the two samples by an approximate calculation. The σ is much larger and D is smaller. So the Li^+ diffusion coefficient of Mn_3O_4-NS/GNS is larger. In other words, the Li^+ diffusion speed of Mn_3O_4-NS/GNS composite is faster in the electrode materials state. It is clear that the increasing of the Li^+ diffusion coefficient is because of the stabile 2D-2D structure of the composite. As expected, the novel 2D-2D structure contributes to decrease the charge transfer resistance and increase the Li^+ diffusion coefficient in the solid phase improving the electrochemical performances.

Besides, the surface area offered by the mica-like Mn_3O_4 and Mn_3O_4-NS/GNS composite are shown in Fig.8. The Brunauer-Emmett-Teller (BET) surface area are estimated to be 40.24 m^2 g^{-1} and 46.89 m^2 g^{-1},[42] which do not change obviously. So, the stability of the Mn_3O_4-NS/GNS composite is again confirmed with 2D-2D sturcture. The 2D structure of Mn_3O_4 nanosheets, stabilising on the graphene (as showed in Fig. S4), which buffer the volume expansion of Mn_3O_4 in the process of lithiation/delithiation.

In short, the stable 2D-2D nanostructure of Mn_3O_4-NS/GNS enhance the electrochemical performances as anode materials for LIBs. This structure can be extended for other electrode materials improving performances.
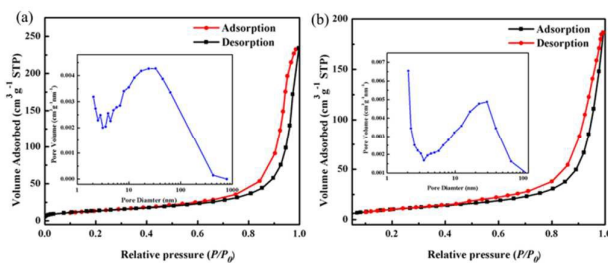
Conclusion

In summary, the 2D-2D Mn_3O_4-NS/GNS composite has been successfully synthesized by a facile approach at room temperature. As an anode materials, the sheet-on-sheet composites show a very large reversible capacity of 1002.95 mA h g^{-1} and superior rate capabilities for LIBs. A high capacity of 659.2 mA h g^{-1} is still observed at a large rate of 1000 mA g^{-1}. The improved electrochemical properties have been ascribed to the increased electrical conductivity and mechanical stability of Mn_3O_4-NS in the presence of GNS. Simultaneously, the GNS are separated and stabilized by Mn_3O_4-NS instead of aggregating, preserving its advantages during repetitive cycling.

Acknowledgements

References

1   P. Poizot, S. Laruelle, S. Grugeon, L. Dupont and J. Tarascon, *Nature*, 2000, **407**, 496–499.
2   Y. P. Gan, H. Q. Gu, H. Xiao, Y. Xia, X. Y. Tao, H. Huang, J. Du, L. S. Xu and W. K. Zhang, *New J. Chem.*, 2014, **38**, 2428–2434.
3   N. D. Petkovich, S. G. Rudisill, B. E. Wilson, A. Mukherjee and A. Stein, *Inorg. Chem.*, 2014, **53**, 1100–1112.
4   H. Gwon, J. Hong, H. Kim, D.-H. Seo, S. Jeon and K. Kang, *Energy Environ. Sci.*, 2014, **7**, 538–551.
5   H. Wang, L. F. Cui, Y. Yang, H. S. Casalongue, J. T. Robinson, Y. Liang, Y. Cui and H. Dai, *J. Am. Chem. Soc.*, 2010, **132**, 13978–13980.
6   F. Ma, A. B. Yuan, and J. Q. Xu, *ACS Appl. Mater. Interfaces*, 2014, **6**, 18129–18138.
7   D. Pasero, N. Reeves and A. R. West, *J. Power Sources.*, 2005, **141**, 156-158.
8   M. J. Aragón, C. Pérez-Vicente and J. L. Tirado, *Electrochem. Commun.,* 2007, **9**, 1744-1748.
9   P. Lavela, J. L. Tirado and C. Vidal-Abarca, *Electrochim. Acta*, 2007, **52**, 7986-7995.
10 J. Gao, M. A. Lowe and H. D. Abruna, *Chem. Mater.*, 2011, **23**, 3223-3227.
11 P. Li, C. Y. Nan, Z. Wei, J. Lu, Q. Peng, and Y. D. Li, *Chem. Mater.*, 2010, **22**, 4232–4236.
12 L. Li, Z. P. Guo, A. J. Du and H. K. Liu, *J. Mater. Chem.*, 2012, **22**, 3600-3605.
13 Pumera. M, *Chem. Soc. Rev.*, 2010, **39**, 4146–4157.
14 S. M. Paek, E. Yoo, and I. Honma, *Nano Lett.*, 2009, **9**,72–75.
15 Y. W. Zhu, S. Murali, W. W. Cai, X. S. Li, J. W. Suk, J. R. Potts, and R. S. Ruoff, *Adv. Mater.*, 2010, **22**, 3906–3924.
16 I. Nam, N. D. Kim, G.-P. Kim, J. Park and J. Yi, *J. Power Sources*, 2013, **244**, 56–62.
17 H. Wang, L.-F. Cui, Y. Yang, H. S. Casalongue, J. T. Robinson, Y. Liang, Y. Cui and H. Dai, *J. Am. Chem. Soc.*, 2010, **132**, 13978–13980.
18 L. Li, Z. Guo, A. Du and H. Liu, *J. Mater. Chem.*, 2012, **22**, 3600–3605.J. W. Lee, A. S. Hall and E. Mallouk, *Chem. Mater.,* 2012, **24**. 1158-1164.
19 C. Chen, H. Jian, X. X. Fu, Z. M. Ren, M. Yan, G. D. Qian and Z.Y. Wang, *RSC Adv.*, 2014, **4**, 5367-5370.
20 Y. Q. Luo, S. S. Fan, N. Y. Hao, S. L. Zhong and W. C. Liu, *Dalton Trans.*, 2014, **43**, 15317-15320.
21 W. W. Sun and Y. Wang, *Nanoscale*, 2014, **6**, 11528-11552.
22 Y. Xia, Z. Xiao, X. Dou, H. Huang, X. H. Lu, and R. J. Yan, etc., *ACS Nano*, 2013, **7**, 7083–7092.
23 Q. Hao, J. Wang, and C. Xu, *J. Mater. Chem. A*, 2014, **2**, 87–93.
24 J. X. Low, S. W. Cao, J. G. Yu, and S. Wageh, *Chem Comm.*, 2014, **50**, 10768-10777.
25 S. K. Park, A. Jin, S. H. Yu, J. Ha, B. Jang, and S. Bong, etc., *Electrochim. Acta*, 2014, **120**, 452–459.
26 A. M. E. Raj, S. G. Victoria, V. B. Jothy, C. Ravidhas, J. Wollschlager, and M. Suendorf, etc., *Appl. Surf. Sci.,* 2010, **256**, 2920-2926.
27 M. V. Reddy, G. Prithvi, K. P. Loh, and B. V. R. Chowdari, *ACS Appl. Mater. Interfaces*, 2014, **6**, 680–690.
28 N. Lavoie, P.R.L. Malenfant, F.M. Courtel, Y. Abu-Lebdeh, and I.J. Davidson, *J. Power Sources*, 2012, **213**, 249-254.
29 S. M. Xu, C. M. Hessel, H. Ren, R. B. Yu, Q. Jin, M. Yang, H. J. Zhao, and D. Wang, *Energy Environ. Sci.,* 2014, **7**, 632–637.
30 D. W. Su, M. Ford, and G. X. Wang, *Sci. Rep.*, 2012, **2**, 924–931.
31 G. Q. Jian, Y. H. Xu, L. C. Lai, C. S. Wang, and M. R. Zachariah, *J. Mater. Chem. A*, 2014, **2**, 4627–4632.
32 X. Wang, X. L. Wu, Y. G. Guo, Y. T. Zhong, X. Q. Cao, Y. Ma, and J. N. Yao, *Adv. Funct. Mater.,* 2010, **20**, 1680–1686.
33 G. M. Zhou, D. W. Wang, F. Li, L. L. Zhang, N. Li, Z. S. Wu, L. Wen, G. Q. Lu, and H. M. Cheng, *Chem. Mater.*, 2010, **22**, 5306-5313.
34 C.B. Wang, L.W. Yin, D. Xiang, and Y.X. Qi, *ACS Appl. Mater. Interfaces*, 2012, **4**, 1636-1642.
35 H. L. Wang, L. F. Cui, Y. Yang, H. S. Casalongue, J. T. Robinson, and Y. Y. Liang et al., *J. Am. Chem. Soc.*, 2010, **132**, 13978–13980.
36 X. J. Ma, Y. J. Zhai, N. N. Wang, J. Yang and Y. T. Qian, *RSC Adv.,* 2015, **5**, 46829-46833.
37 Y. R. Ren, J. We. Wang, X. B. Huang, B. Yang, and J. N. Ding, *RSC Adv.*, 2015, **5**, 59208-59217.
38 X. W. Li, L. Qiao, D. Li, X. H. Wang, W. H. Xie, and D. Y. He, *J. Mater. Chem. A*, 2013, **1**, 6400–6406.
39 A.J. Bard and L.R. Faulkner, *Electrochemical Methods*, Wiley, NewYork, 2001, p. 231.
40 X. Y. Shan, G. M. Zhou, L. C. Yin, W. J. Yu, F. Li, and H. M. Cheng, *J. Mater. Chem. A*, 2014, **2**, 17808–17814.
41 J. J. Duan , S. Chen , S. Dai , and S. Z. Qiao, *Adv. Funct. Mater.*, 2014, **24**, 2072–2078.
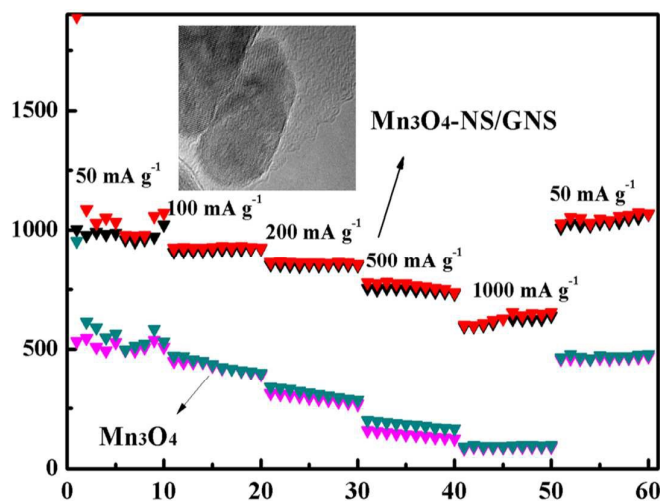
The 2D-2D nanostructured composite of Mn_3O_4 nanosheet stabilising on graphene sheet presents the enhanced electrochemical performances.